

## Article

# Modeling and Simulation of Single Flow Zinc–Nickel Redox Battery Coupled with Multi-Physics Fields

Chunning Song \* , Kaixuan Zhang and Nanjun Li

School of Electrical Engineering, Guangxi University, Nanning 530004, China; zhangkaixuancz@163.com (K.Z.); nanjun181@163.com (N.L.)

\* Correspondence: scn206@gxu.edu.cn; Tel.: +86-135-1788-0082

**Abstract:** Metallic zinc (Zn) presents a compelling alternative to conventional electrochemical energy storage systems due to its environmentally friendly nature, abundant availability, high water compatibility, low toxicity, low electrochemical potential ( $-0.762$  V vs. SHE), and cost-effectiveness. While considerable efforts have been devoted to enhancing the physical and chemical properties of zinc-ion battery materials to improve battery efficiency and longevity, research on multi-physics coupled modeling for a deeper understanding of battery performance remains relatively scarce. In this study, we established a comprehensive two-dimensional model for single-flow zinc–nickel redox batteries to investigate electrode reactions, current-potential behaviors, and concentration distributions, leveraging theories such as Nernst–Planck and Butler–Volmer. Additionally, we explored the distribution of the velocity field using the Brinkman theory in porous media and the Navier–Stokes equations in free-flow channels. The validated model, informed by experimental data, not only provides insights into the performance of the battery, but also offers valuable recommendations for advancing single-flow zinc–nickel battery technology. Our findings offer promising avenues for enhancing the design and performance of not only zinc–nickel flow batteries, but also applicable for other flow battery designs.

**Keywords:** single-flow zinc–nickel redox battery; redox flow battery; numerical simulation; finite element analysis; concentration distribution; current-potential behavior



**Citation:** Song, C.; Zhang, K.; Li, N. Modeling and Simulation of Single Flow Zinc–Nickel Redox Battery Coupled with Multi-Physics Fields. *Batteries* **2024**, *10*, 166. <https://doi.org/10.3390/batteries10050166>

Academic Editors: Chunwen Sun and Leon L. Shaw

Received: 4 April 2024

Revised: 23 April 2024

Accepted: 14 May 2024

Published: 19 May 2024



**Copyright:** © 2024 by the authors. Licensee MDPI, Basel, Switzerland. This article is an open access article distributed under the terms and conditions of the Creative Commons Attribution (CC BY) license (<https://creativecommons.org/licenses/by/4.0/>).

## 1. Introduction

Energy plays an increasingly crucial role with the rapid development of the socio-economic landscape. Over-reliance on fossil fuels has led to significant challenges in global energy and ecological environments [1]. To address this trend, there is a growing demand for electricity generation from renewable energy sources such as wind, solar, and tidal energy. However, renewable energy sources are often intermittent and uncontrollable, posing challenges in maintaining a stable power level. Batteries, as reliable and reversible energy storage systems, have garnered widespread attention [2].

Currently, lithium-ion batteries have dominated the energy storage market [3,4]. However, issues related to the high cost [5], limited reserves of lithium mineral resources [6], and safety concerns arising from the use of flammable organic electrolytes in lithium-ion batteries cannot be ignored [7,8]. The cost and safety issues associated with lithium-ion batteries have become significant. In comparison to non-aqueous organic electrolytes, aqueous electrolytes are safer, more abundant, environmentally friendly, exhibit higher ionic conductivity, have lower costs, and are easier to manufacture [9]. Lead-acid batteries, representing aqueous rechargeable batteries, have been widely used due to advantages, such as their inherent safety and low cost. However, critical drawbacks, including low energy density, large volume and mass, and high toxicity of lead compounds, cannot be neglected [10]. Therefore, there is an urgent need to develop the next generation of electrochemical energy storage devices that possess inherent safety as alternatives to lead-acid batteries [11].

The electrochemical insertion/deinsertion of multivalent cations like  $Zn^{2+}$ ,  $Mg^{2+}$ ,  $Ca^{2+}$ , and  $Al^{3+}$  has gained increasing attention as a potential system for multi-electron transfer batteries [12,13]. Among them, zinc (Zn) metal has received considerable attention due to its suitable potential [14] ( $-0.76$  V vs. standard hydrogen electrode (SHE)), higher mass/volume capacity [15] (820 mAh/g and 5855 mAh/cm<sup>3</sup>), moderate reversibility with fast kinetics [16] ( $k_0$  for  $Zn(OH)_4^{2-}/Zn$  is  $2.5 \times 10^{-4}$  cm/s), abundant reserves [17], low-toxicity compounds [18], and low cost [16] (1.9 \$/kg). Therefore zinc-based aqueous ion batteries or metal batteries have been continuously explored. Zinc–nickel redox flow batteries (RFB), as one of the deposition type single flow battery, have attracted extensive attention from researchers due to their merits such as being membraneless, having low cost, high efficiency, and convenience in assembly since it was invented in 2007 [19]. Zinc–nickel RFBs belong to the aqueous zinc-based flow battery system, which is a relatively unique type among various RFB. Typically, the electrolytes used in the positive and negative electrodes of flow batteries are different substances, and measures need to be taken to prevent cross-contamination between the two electrolytes. Therefore, an ion exchange membrane is required to separate the electrolytes between the positive and negative electrodes. However, the same electrolyte solution can be used for both the positive and negative electrodes, which means issues related to membrane lifespan, electrolyte cross-contamination, and their impact on coulombic efficiency is mitigated for zinc–nickel RFBs, which no longer need to meet the requirement for expensive ion exchange membranes, thereby reducing industrial costs. In addition, the flowing electrolyte can inhibit the deposition of unreactive “dead-zinc” and the notorious zinc dendrites formation to some extent during the charging process, which increase operational efficiency as well as battery life span [20].

This study endeavors to construct and authenticate a comprehensive model of zinc–nickel RFBs. In recent years, zinc–nickel RFBs have received increasing interest since their inception. Extensive experimental investigations have focused on electrode materials [21,22], electrode morphology [23–26], and electrolyte additives [27–29] to improve battery performance, efficiency, and lifespan. However, most scholars focus on optimizing the physical and chemical properties of battery materials to improve the efficiency and lifespan of batteries, while research on the multi-physics coupled modeling to develop the understanding of batteries performance is not very common. Some scholars have simulated the dendrite growth [30], as well as hydrogen evolution [31], in zinc–nickel RFBs by means of a lattice Boltzmann or mathematical model. The results of numerical simulation of the equivalent circuit model and the electrochemical model suggest inspiring conclusions [32,33]. Techniques with density functional theory calculations [34] are utilized in organic RFBs to predict potential, albeit they are not applicable to zinc–nickel RFBs yet. As mentioned in Ref. [35], investigating the numerical processes of zinc–nickel RFBs is one potential future direction.

In this study, a two-dimensional transient model integrating all three transport modes (migration, diffusion, and convection), along with electrode kinetics, is developed for zinc–nickel RFBs. The model undergoes validation through the galvanostatic charge/discharge process with an assembled battery prototype. Drawing from these simulation outcomes, crucial suggestions are made for achieving high performance and for guiding future advancements in zinc–nickel RFB technology.

## 2. Model Description

As shown in Figure 1, a zinc–nickel RFB is composed of a porous nickel positive electrode, a negative electrode for zinc deposition and reaction, a reservoir for electrolyte storage, pipes connecting the reservoir and battery prototype, and a pump for electrolyte circulation. Battery pictures are shown in Section 2.2.2. The horizontal direction corresponds to thickness of the electrode. The vertical direction is the electrode height direction, as well as the electrolyte flow direction along the channel. Both zinc deposition/stripping and hydrogen evolution are considered to occur on the surface of the negative electrode, while on the positive electrode, both the  $NiOOH/Ni(OH)_2$  redox reaction and oxygen evolution

occur. The model accounts for the transport of charged species through electrolytes by diffusion, migration, and convection. The negative electrode boundary serves as a reference node to ground, and its potential is set to zero.

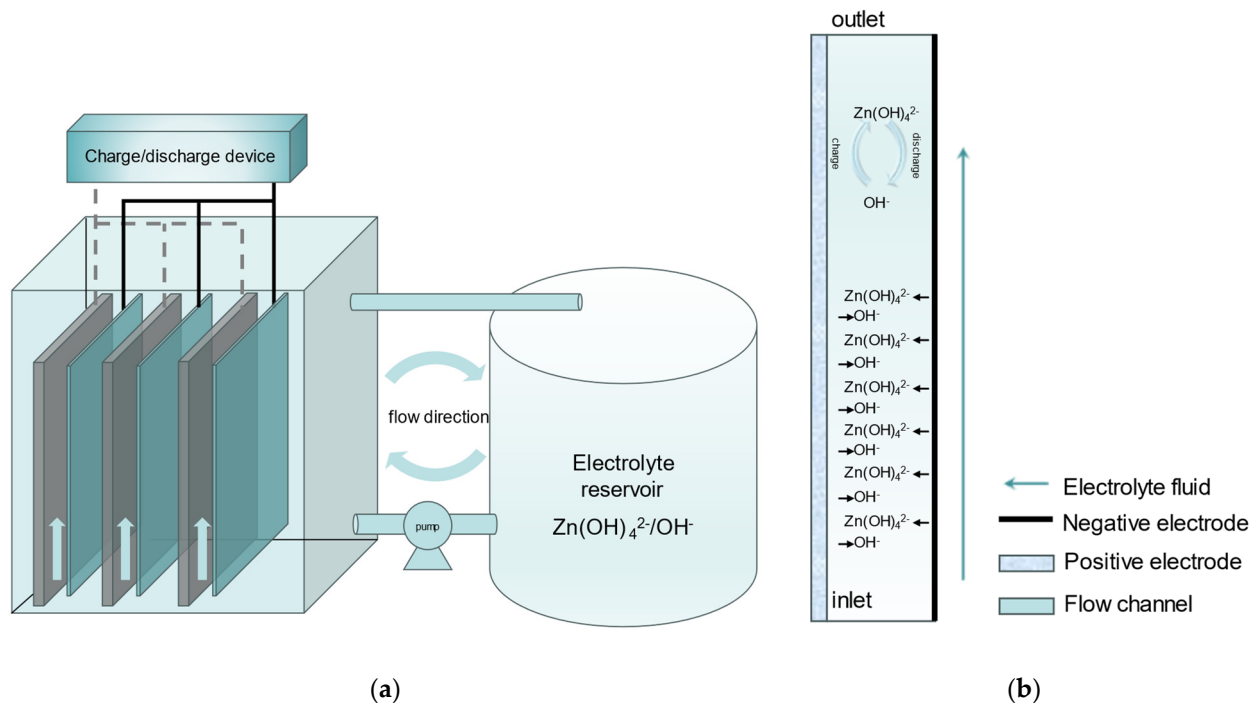
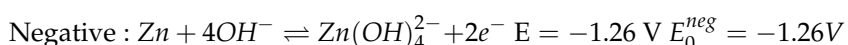
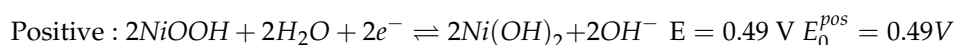


**Figure 1.** (a) Schematic diagram of the structure of Zn-Ni RFB; (b) Schematic <sup>1</sup> working principle of Zn-Ni RFB. <sup>1</sup> Schematic do not represent the actual dimensions after being scaled proportionally.

The main electrochemical reactions that occur in the alkaline battery system for the positive and negative electrode are listed as follows:



The reaction mechanism of zinc–nickel RFB during operation is described as follows. During discharge, zinc previously deposited on the negative electrode loses electrons and consumes hydroxide ions ( $OH^-$ ) from the electrolyte solution, forming  $Zn(OH)_4^{2-}$ . At the same time, nickel oxyhydroxide ( $NiOOH$ ) in the positive electrode receiving electrons and being reduced to  $Ni(OH)_2$  while generating  $OH^-$ . The high concentration of  $OH^-$  ions near the positive electrode in the solution flows along the concentration gradient towards the negative electrode area with a lower  $OH^-$  concentration. Simultaneously, due to the circulation flow of the circulation pump, the concentration polarization phenomenon in zinc–nickel RFB is alleviated, which can also inhibit the growth of zinc dendrites. During charging,  $Ni(OH)_2$  at the positive electrode consumes  $OH^-$  ions and loses electrons, and can be oxidized to  $NiOOH$ , while  $Zn(OH)_4^{2-}$  ions near the negative electrode receive electrons and are reduced to  $Zn$ , with  $OH^-$  simultaneously generated.

The electrolytes are supplied from the reservoir, which pumps the electrolyte into the channels subsequently and flow to the exit through the electrodes. Finally, the electrolytes flow back to the reservoir until next circulation. The geometrical parameters of the zinc–nickel RFB are presented in Table 1.

**Table 1.** The geometric parameters of zinc–nickel RFB.

Symbol	Parameter Definition	Value
H	Height of battery	240 mm
$L_1$	Thickness of positive electrode	0.64 mm
$L_2$	Width of channel	4.44 mm
$W^2$	Length of electrodes	160 mm

<sup>2</sup> The length is used to calculate the active area of the electrode and is not shown in Figure 2.

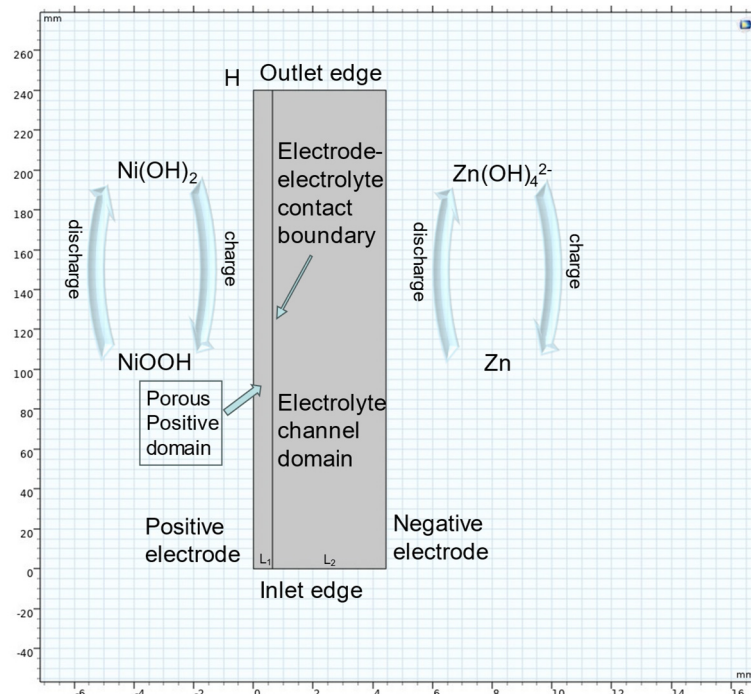
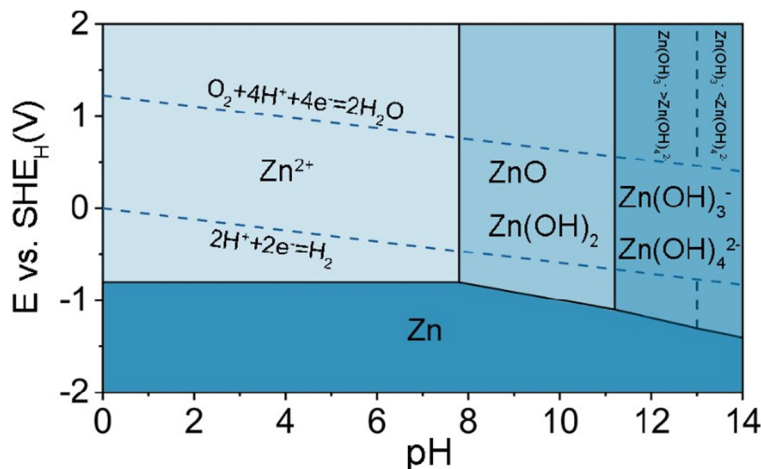
**Figure 2.** Model of a pair of electrodes of battery stack in COMSOL Multiphysics.

Figure 2 shows the schematic diagram for modeling a pair of electrodes of zinc–nickel RFB in COMSOL Multiphysics.

The main assumed conditions of this model are listed as follows:

1. The physical properties of the electrode and electrolyte are isotropic and constant, and the effects of temperature and side reactions are not considered.
2. The model neglects the potential gradient within the electrode collector, and the model excludes the electrode collector.
3. Assuming that zinc-related reactions only occur on the electrode surface in contact with the electrolyte, the current density distribution on the surface of electrode plate is considered to be uniform.
4. The transformation process of positive-electrode-active material ( $\text{NiOOH}/\text{Ni}(\text{OH})_2$ ) in the charge–discharge process is regarded as the process of proton generation and transmission in the solid-phase.
5. The electrolyte is a dilute solution mixed fully and evenly in the reservoir, and the flow of electrolyte between the plate is incompressible laminar flow.
6. The negative electrode is considered as a boundary with zero thickness and grounded to zero potential.
7. According to the pourbaix diagram of Zn in aqueous solution, as Figure 3 shows, intermediate reactions are not considered due to the strong alkalinity of the solution.



**Figure 3.** Pourbaix diagram of Zn in an aqueous solution [36].

## 2.1. Governing Equations and Boundary Conditions

The governing equation of the model consists of convective flow equations, mass transfer equations, charge migration equations, and electrochemical kinetics. The mass transfer and charge migration equations in the porous positive electrode are divided into a solid phase and a liquid phase. Detailed descriptions will be provided in Sections 2.1.2 and 2.1.4.

### 2.1.1. Convective Flow

The electrolyte flow was characterized by employing the Navier–Stokes equations to model the flow in the free-flow region, while the Brinkman equation was utilized to represent the flow within the porous positive-electrode region. To ensure mass conservation, both the continuity equation and the momentum equation were applied.

$$\rho(v \cdot \nabla)v = -\nabla p + \nabla \cdot [\mu(\nabla v + (\nabla v)^T)] + F_{ex} \quad (1)$$

$$\frac{\rho}{\varepsilon} \left( \frac{\partial v}{\partial t} + (v \cdot \nabla) \frac{v}{\varepsilon} \right) = -\nabla p + \nabla \cdot \left\{ \frac{\mu}{\varepsilon} \left[ (\nabla v + (\nabla v)^T) - \frac{2}{3}(\nabla \cdot v)I \right] \right\} - \left( \frac{\mu}{\kappa} + \frac{Q_m}{\varepsilon^2} \right) v + F_{ex} \quad (2)$$

$$\rho(v \cdot \nabla)v = 0 \quad (3)$$

where  $\rho$  is the electrolyte density,  $v$  is the local flow velocity,  $p$  is the pressure,  $\mu$  is the dynamic viscosity of electrolyte,  $\varepsilon$  is the porosity of positive electrode,  $\kappa$  is the permeability of the fluid through the porous electrodes,  $Q_m$  is the mass source accounts for mass deposit and mass creation within the domains calculated by Equation (4),  $I$  stands for unit tensor, and  $F_{ex}$  stand for the external forces as constant 0 in this paper.

$$\nabla \cdot (\rho v) = Q_m \quad (4)$$

Since the flow of electrolyte is regarded as incompressible laminar flow with uniform velocity, the Brinkman equations can be simplified as:

$$\frac{\rho}{\varepsilon} \left( (v \cdot \nabla) \frac{v}{\varepsilon} \right) = -\nabla p + \nabla \cdot \left\{ \frac{\mu}{\varepsilon} \left[ (\nabla v + (\nabla v)^T) - \frac{2}{3}(\nabla \cdot v)I \right] \right\} - \left( \frac{\mu}{\kappa} + \frac{Q_m}{\varepsilon^2} \right) v \quad (5)$$

### 2.1.2. Mass Transfer

Mass transfer governs the transportation of ions in the electrolyte containing  $i = \{Zn(OH)_4^{2-}, OH^- \}$  and the build-up of zinc hydroxide at the anode. Mass transfer in the

electrolyte is described by the mass conservation equation, which yields as Equation (6) for different ions:

$$\frac{\partial c_i}{\partial t} + \nabla \cdot \vec{N}_i = 0 \quad (6)$$

where  $c_i$  and  $\vec{N}_i$  are the concentration and molar flux of species  $i$ , respectively. The flux of a species in an electrolyte under the influence of diffusion, migration, and convection is given by the Nernst–Planck equation:

$$\vec{N}_i = -D_i \nabla c_i - \frac{z_i F}{RT} D_i c_i \nabla \varphi_l + c_i \vec{v} \quad (7)$$

where  $D_i$  and  $z_i$  are the diffusion coefficient and charge number of species  $i$ , respectively.  $F$  is the Faraday constant,  $R$  is the gas constant,  $T$  is the temperature, and  $\varphi_l$  is the potential of electrolyte.

In porous electrodes, the conservation of mass on the positive side is different. Taking porosity into consideration, Equation (6) can be written as:

$$\frac{\partial (\varepsilon c_j)}{\partial t} + \nabla \cdot \vec{N}_j = S_j \quad (8)$$

where  $S_j$  is the source term due to the electrochemical reaction occurring on the cathode, given by Equation (9):

$$S_j = \sum \frac{A v_j j}{n F} \quad (9)$$

where  $A$  is the active specific surface area and  $v_j$  is the stoichiometric coefficient of species  $j = \{H^+, Zn(OH)_4^{2-}, OH^- \}$  in the reaction. For different ions, the substance source terms involved are shown in Table 2 below.

**Table 2.** Species source term of zinc–nickel RFB.

Source Terms	Species	Positive	Negative
$S_{neg}$	$OH^-$	$- A j_{loc}/F$	$2 j_{loc}/F$
	$Zn(OH)_4^{2-}$	0	$j_{loc}/2F$
$S_{pos}$	$H^+$	$- A j_{loc}/F$	0

Where  $j_{loc}$  is the local charge transfer current density in the negative and positive electrodes, illustrated in Section 2.1.3.

In porous electrodes, the concentration distribution of different kinds of ions is calculated based on the Nernst–Planck equation with the effective parameters:

$$\vec{N}_j = -D_j^{eff} \nabla c_j - \frac{z_j F}{RT} D_j^{eff} c_j \nabla \varphi_l + c_j \vec{v} \quad (10)$$

The effective diffusion coefficient  $D_j^{eff}$  of species  $j$  considers the porosity  $\varepsilon$  of the positive electrode and is related to the molecular diffusion coefficient  $D_j$  through the Bruggemann correction:

$$D_j^{eff} = \varepsilon^{1.5} D_j \quad (11)$$

Due to the incompressibility condition, the continuity equation shown in Equation (3) is also valid on the positive side. The flow velocity of liquid in porous media is typically described by Darcy's law, given by:

$$v = -\frac{\kappa}{\mu} \nabla p \quad (12)$$

### 2.1.3. Electrochemical Kinetics

For reactions take place on the surface of electrode, equilibrium potential is given by the Nernst equation:

$$E^{eq} = E_0^{eq} + \frac{RT}{nF} \ln\left(\frac{c_{ox}}{c_{re}}\right) \quad (13)$$

where  $E_0^{eq}$  represent the standard equilibrium potential of electrochemical reactions,  $c_{ox}$  and  $c_{re}$  are concentration of oxidized mass and reduced mass, respectively. The value of  $n$  represents the number of electrons transferred during the reaction. For the negative electrode,  $n$  is equal to 2, while for the positive electrode,  $n$  equals 1.

The electrochemical reactions occurring at the electrode surface are governed by the Butler–Volmer equation, which relies on the surface concentrations and reference concentrations of the chemical species. Consequently, the local charge transfer current density per unit volume in the negative and positive electrodes can be defined as follows:

$$j_{loc} = A j_0 \left[ \prod \left( \frac{c_{re}}{c_{re,ref}} \right)^{\nu_a} \exp\left(\frac{\alpha_a n F}{RT} \eta\right) - \prod \left( \frac{c_{ox}}{c_{ox,ref}} \right)^{\nu_c} \exp\left(\frac{-\alpha_c n F}{RT} \eta\right) \right] \quad (14)$$

Here,  $\eta$  is the electrode overpotentials for the positive and negative side,  $\nu_a$  and  $\nu_c$  are the stoichiometric coefficient which are positive for products and negative for reactants in a reduction reaction, and  $\alpha_a$  and  $\alpha_c$  are the anode and cathode transfer coefficients, respectively obeying the following Equation:

$$\alpha_a + \alpha_c = \frac{n}{\nu} \quad (15)$$

For reactions occurring in Zn-Ni RFB, the sum of anode transfer coefficients  $\alpha_a$  and cathode transfer coefficients  $\alpha_c$  equals 1.

The exchange current densities  $j_0$  are defined as:

$$j_0 = n F k (c_{ox})^{\alpha_a} (c_{re})^{\alpha_c} \quad (16)$$

where  $k$  represent the reaction rate constants on electrodes.

The activation overpotentials  $\eta$  in Equation (14) is calculated as follows:

$$\eta = \varphi_s - \varphi_l - E^{eq} \quad (17)$$

where  $\varphi_s$  and  $\varphi_l$  are the potential of the solid electrode and the potential of the electrolyte in contact with the electrode, which will be discussed in detail in Section 3.4, and  $E^{eq}$  is evaluated using Equation (13). Table 3 outlines the constants related to ion transport and the electrochemical parameters associated with transport used in the mathematical model proposed in this study, with some data sourced from the literature.

**Table 3.** The constants related to the ion transport and electrochemistry parameters [37].

Symbol	Parameter Definition	Value
$D_{Zn(OH)_4^{2-}}$	Diffusion coefficient of $Zn(OH)_4^{2-}$	$3.10 \times 10^{-10} \text{ m}^2/\text{s}$
$D_{H^+}$	Diffusion coefficient of $H^+$	$9.31 \times 10^{-9} \text{ m}^2/\text{s}$
$D_{OH^-}$	Diffusion coefficient of $OH^-$	$5.26 \times 10^{-9} \text{ m}^2/\text{s}$
$\alpha_a^{neg}$	Anodic transfer coefficients of negative reaction	0.5
$\alpha_a^{pos}$	Anodic transfer coefficients of positive reaction	0.5
$\alpha_c^{neg}$	Cathodic transfer coefficients of negative reaction	0.5
$\alpha_c^{pos}$	Cathodic transfer coefficients of positive reaction	0.5
$E_0^{neg}$	Standard potential of negative reaction	-1.26 V
$E_0^{pos}$	Standard potential of positive reaction	0.49 V
$k_{neg}$	Reaction rate constant of negative reaction	$2.5 \times 10^{-6} \text{ m/s}$
$k_{pos}$	Reaction rate constant of positive reaction	$4 \times 10^{-8} \text{ m/s}$

#### 2.1.4. Electrolyte Potential and Electrode Potential

The concentrations of the species within the electrolyte are linked with the electroneutrality condition:

$$\sum_i z_i c_i = 0 \quad (18)$$

The current density produced by the flux of each charged species  $i$  in the electrolyte is:

$$\vec{j}_i = z_i F \vec{N}_i \quad (19)$$

Substitution of Equation (6) into Equation (19) yields:

$$\vec{j}_i = z_i F (-D_i \nabla c_i) + z_i F \left( -\frac{z_i F}{RT} D_i c_i \nabla \varphi_l \right) + z_i F (c_i \vec{v}) \quad (20)$$

The total current density across the electrolyte is obtained as:

$$\vec{j}_l = \sum_i \vec{j}_i = F \sum_i \left[ z_i (-D_i \nabla c_i) - \frac{F}{RT} (z_i^2 D_i c_i \nabla \varphi_l) + z_i (c_i \vec{v}) \right] \quad (21)$$

The electromigration term in the above Equation can be expressed as follows:

$$j = -\sigma_l \nabla \varphi_l, \sigma_l = \frac{F^2}{RT} \sum_i z_i^2 D_i c_i \quad (22)$$

The electrode current density  $j_s$  in the positive solid electrode is obtained using Ohm's law:

$$\vec{j}_s = -\sigma_s^{eff} \nabla \varphi_s \quad (23)$$

where  $\varphi_s$  is the potential of porous positive electrode,  $\sigma_s^{eff}$  is the effective electrical conductivity of the porous electrode, which accounts for the porosity and is related to the intrinsic conductivity  $\sigma_s$  of the electrode material, and is adjusted by the Bruggman correction:

$$\sigma_s^{eff} = \varepsilon^{1.5} \sigma_s \quad (24)$$

Conservation of charge about the electrolyte and electrode is given by:

$$\nabla \cdot \vec{j}_l = F \sum_i (z_i S_i) \quad (25)$$

$$\nabla \cdot \vec{j}_s = \nabla \cdot (-\sigma_s^{eff} \nabla \varphi_s) \quad (26)$$

where  $S_i$  includes all source terms related with electrochemical reactions carried out in the surface of the porous positive electrode.

Due to the conservation of charge, the divergence of the total current density equals 0:

$$\nabla \cdot \vec{j} = \nabla \cdot \vec{j}_l + \nabla \cdot \vec{j}_s = 0 \quad (27)$$

Table 4 outlines the physical and chemical constants used in simulation, with some data sourced from the literature.

**Table 4.** The physical and chemical constants used in simulation <sup>3</sup> [30,38].

Symbol	Quantity Parameter Definition	Value
$T$	Temperature	293.15 K
$F$	Faraday constant	96,485 C/mol
$R$	Molar gas constant	8.314 J/(mol·K)
$\rho$	Density of electrolyte	1456.1 kg/m <sup>3</sup>
$\mu$	Dynamic viscosity of electrolyte	0.03139 Pa·s
$\epsilon$	Porosity of electrode	0.44
$\kappa$	Permeability of electrode	$3.75 \times 10^{-12}$ m <sup>2</sup>
$\sigma_s$	Conductivity of electrode	2500 s/m
$\sigma_l$	Conductivity of electrolyte	65 s/m
$c_{Zn(OH)_4^{2-}}^{ref}$	Reference concentration of Zn(OH) <sub>4</sub> <sup>2-</sup>	1.5 mol/dm <sup>3</sup>
$c_{Zn}^{ref}$	Reference concentration of Zn	1 mol/dm <sup>3</sup>
$c_{OH^-}^{ref}$	Reference concentration of OH <sup>-</sup>	7.1 mol/dm <sup>3</sup>

<sup>3</sup> All parameters related to the electrode mentioned in Table 4. Refer to properties of porous positive electrode.

### 2.1.5. Boundary Conditions

At the inlet of flow, it is configured so that the concentration of each species is constant, and the mass transport boundaries conditions are defined as:

$$c_m^{in} = c_m^0, y = 0 \quad (28)$$

where  $c_m^{in}$  is the concentration of  $m$  species at the inlets, while  $c_m^0$  is the initial concentration listed in Table 5.

**Table 5.** Basic operational parameters and initial condition settings.

Symbol	Quantity Parameter Definition	Value
$c_{Zn(OH)_4^{2-}}^0$	initial Zn(OH) <sub>4</sub> <sup>2-</sup> concentration	1 mol/dm <sup>3</sup>
$c_{OH^-}^0$	initial OH <sup>-</sup> concentration	10 mol/dm <sup>3</sup>
$A$	active specific surface area	384 cm <sup>2</sup>
$V$	Volume between a pair of electrode plates	195 cm <sup>3</sup>
$V_{cell}$	cell-voltage	1.2–2.0 V
$i_{app}$	applied current density	set
$Q$	volumetric flow rate	max 8 L/min
$p$	pressure	0

With regard to the conservation of momentum at the electrolyte entries, constant flow velocities are applied as boundary conditions, as described below:

$$\vec{v} = -v^{in} \cdot \vec{n}, y = 0 \quad (29)$$

$$v_{in} = \frac{Q}{(L_1 + L_2)W}, y = 0 \quad (30)$$

where  $\vec{n}$  denotes the outward unit normal vector.

At the exits of the channel, the diffusive fluxes of all the species are expected to be zero:

$$-D_i \nabla c_i \cdot \vec{n} = 0, y = H \quad (31)$$

The pressure can be taken as constant:

$$p = p_{out}, y = H \quad (32)$$

The boundary condition at negative electrode is to be grounded to zero potential, and a potential is established on the surface of the porous positive electrode, described as:

$$\varphi_s = 0, x = L_1 + L_2 \quad (33)$$

$$\varphi_s = V_{cell}, x = 0 \quad (34)$$

The battery is operated galvanostatically in this study. Thus, the negative electrode is grounded and the current density at each electrode is set to the applied current density.

$$i = i_{app} \text{ (during charge)} \quad (35)$$

$$i = -i_{app} \text{ (during discharge)} \quad (36)$$

Assuming that the electrolyte is fully and evenly mixed, the inlet concentrations of  $c_{Zn(OH)_4^{2-}}$  and  $c_{OH^-}$  are controlled by the ordinary differential Equations (35) and (36), as follows:

$$\frac{\partial c^{in}}{\partial t} = \frac{H}{V} \left( \int_{out} (\vec{N} \cdot \vec{n}) ds - \int_{in} (\vec{N} \cdot \vec{n}) ds \right) \quad (37)$$

$$c = c^0 - \int_0^t \frac{\partial c^{in}}{\partial t} \quad (38)$$

where  $V$  denotes the volume between a pair of electrode plates.

It should be noted that no-slip walls are assumed for the wall boundary of the flow frame, which ensures that there is no electrolyte leakage through these surfaces.

## 2.2. Model Calculations and Experimental Details

### 2.2.1. Model Calculations

This paper uses COMSOL Multiphysics® v. 6.0. software (COMSOL) to simulate the model with the finite-element method. The electrolyte flow was simulated by the “laminar flow interface” and the mass transfer equations, potential distribution, and electrode dynamics equations are calculated by the “tertiary current distribution-Nernst–Planck interface”. A mapped rectangular grid is used in the model. Meanwhile, boundary grid demarcation is used to resolve the steep gradient in the electrolyte near the electrode surface. The geometric model is divided into 3480 units using arithmetic progression, and a total of 19,605 degrees of freedom were calculated. The relative tolerance of model calculation was set as  $10^{-6}$ . The set of geometric parameters are listed in Table 1, the constants related to the ion transport and electrochemistry parameters are given in Table 3, and Table 4 provides the physical and chemical constants used in the simulation. Basic operational parameters and initial condition settings are listed in Table 5.

### 2.2.2. Experimental Details

In this study, a single-flow zinc–nickel battery consisting of a pair of one positive plate and one negative plate with a theoretical capacity of 8 A·h was built for experiment. The dimensions of the porous positive plate were 240 mm × 160 mm × 0.64 mm (height × width × thickness), and for the negative plate, the measures were 240 mm × 160 mm × 0.08 mm. Electrodes are shown in Figure 4a, and the model matches the side view of assembled battery as Figure 4b shows, with the electrolyte inlet at the bottom and the outlet at the top. On the left is a nickel-oxide-based positive electrode plate, and on the right is a nickel-plated perforated steel strip negative electrode with holes. After mixing 10 M KOH solution with 1 M LiOH solution, the electrolyte is prepared by adding 81.4 g (1 mole) of ZnO per liter of solution, forming  $Zn(OH)_4^{2-}/OH^-$  for redox reaction. The charge/discharge device was a CT-3004-5V200A-NTFA battery test platform manufactured by Newware Electronics Co., Ltd. (Shenzhen, China). It is notable that during actual battery

operation, the first process is to charge to allow some zinc to deposit on the electrode surface before starting the charge–discharge cycle since there is no activated zinc available for reaction on the plate.

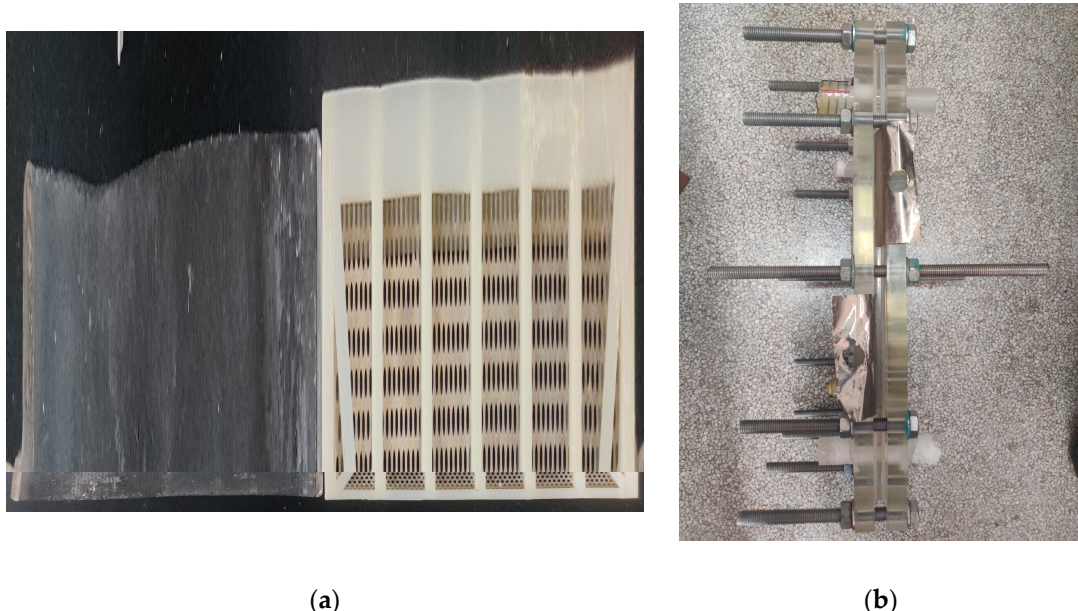


**Figure 4.** (a) On the left side is the nickel-oxide-based positive electrode plate; on the right is a nickel-plated perforated steel strip negative electrode with holes. (b) Assembled zinc–nickel RFB prototype with a pair of electrodes.

### 3. Results and Discussion

Four parts are included in this chapter: validation of the proposed model, hydrodynamics analysis, concentration distribution, and current-potential behavior of the zinc–nickel RFB. In Section 3.1, the validity of the model is demonstrated by comparing the simulation results with the experimental data in one round of cycling. Section 3.2 delves into hydrodynamic analysis across different regions of the zinc–nickel RFB. The concentration distribution of different ions is illustrated in Section 3.3. Lastly, Section 3.4 utilizes the simulated current-potential distribution to elucidate the electrochemical behavior of zinc–nickel RFB.

#### 3.1. Validation of the Model

In order to verify the accuracy of the model, galvanostatic charge/discharge cycle experiments were carried out on the experimental battery at room temperature. The battery charge/discharge device is the CT-3004-5V200A-NTFA battery test platform manufactured by Shenzhen Newware Electronics Co., Ltd. The current density and charge/discharge time were set as  $10 \text{ mA/cm}^2 \times 14,400 \text{ s}$  (4 h),  $20 \text{ mA/cm}^2 \times 7200 \text{ s}$  (2 h), and  $40 \text{ mA/cm}^2 \times 3600 \text{ s}$  (1 h), correspondingly. Eventually, a battery in all three conditions get the same electric charge ( $7.68 \text{ A}\cdot\text{h}$ ), according to Equation (39):

$$Q_e = A i_{app} t \quad (39)$$

where  $Q_e$  is the actual capacity of electric charge of a pair of electrodes in the zinc–nickel RFB battery used in this study. It is notable that the total time half consists of charging time and half of discharging time.

The output voltage experimental curve and numerical simulation curve under three different charge–discharge constant current input conditions are shown in Figure 5, which depicts the simulated and experimental plots of cell voltage vs. time at current densities of 10, 20, and  $40 \text{ mA/cm}^2$ . The curve operated at  $20 \text{ mA/cm}^2$  current density is used to

illustrate the validity of the model. It should be noted that the experimental battery voltage output curve, shown in Figure 5b, corresponds to the second charge/discharge cycle during battery operation since the first one serves as a preconditioning step, including a 20 min static rest and the first round of battery charging activation, which means that the first cycle does not accurately characterize the battery performance.

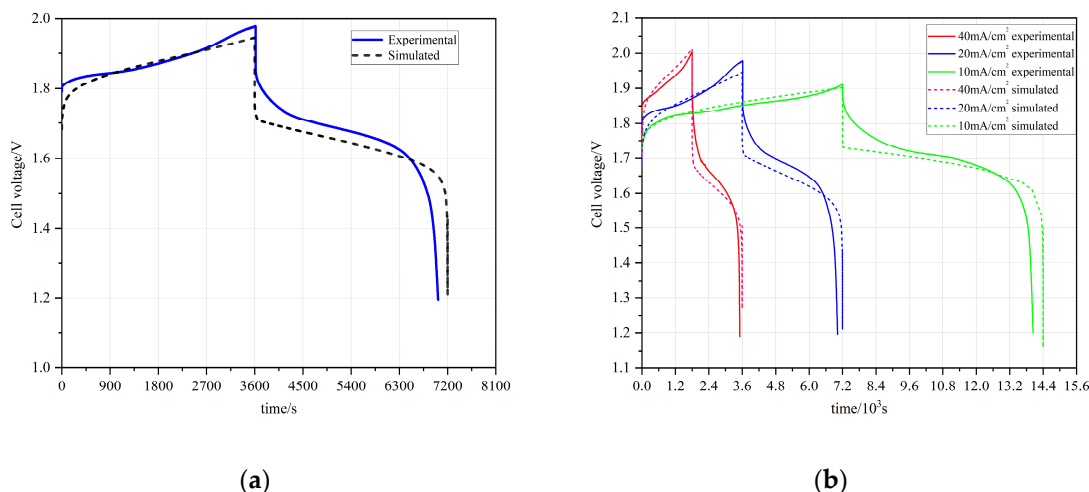
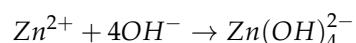
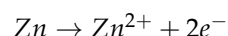
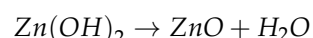
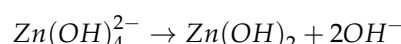


**Figure 5.** (a) Simulated and experimental curve of a zinc–nickel RFB cell voltage operating at  $20 \text{ mA}/\text{cm}^2$  with 2 h charge–discharge process. (b) Comparison of simulated and experimental battery voltage under different applied current densities ( $10 \text{ mA}/\text{cm}^2$ ,  $20 \text{ mA}/\text{cm}^2$ , and  $40 \text{ mA}/\text{cm}^2$ ).

At  $10 \text{ mA}/\text{cm}^2$ , the maximum voltage simulated using the proposed model is  $2.0045 \text{ V}$ , while experimental data is  $2.01354 \text{ V}$ , expressed as simulated voltage/experimental voltage, and it drops to  $1.94576 \text{ V}/1.9788 \text{ V}$  at  $20 \text{ mA}/\text{cm}^2$  and  $1.90151 \text{ V}/1.9109 \text{ V}$  at  $40 \text{ mA}/\text{cm}^2$ , respectively. As previously research demonstrated [39], with increased current density, the electrochemical polarization intensifies, the polarization resistance increases, and the output voltage decreases. The simulation results show a sudden decrease in voltage, while the experimental results exhibit a relatively slower decline in voltage. This is due to the fact that the model only considers a single-step reaction:  $\text{Zn(OH)}_4^{2-}$  formed during the zinc oxidation process combine with hydroxide ions, as shown in Section 2. In fact, the negative electrode undergoes a multi-step reaction during the discharge process [40]:



In addition,  $\text{Zn(OH)}_4^{2-}$  can react to form  $\text{Zn(OH)}_2$  and further dehydrates to form  $\text{ZnO}$ , which deposits on the electrode surface, increasing the resistance of the battery and hindering the reaction process.



The formation of  $\text{Zn(OH)}_2$  and its subsequent deposition on the negative electrode offers additional resistance to the cell reaction, thereby reducing the discharge potential. Hence a sudden drop in potential is not observed in the experimental results.

While there is not a perfect alignment between the experimental and simulation outcomes, the model's steady-state operation results appear to be accurate, providing satisfactory precision for subsequent applications. The validation of the model against experimental data not only enabled the prediction of battery operation status, but also facilitated the identification of the dominant redox reaction under various operational scenarios.

### 3.2. Hydrodynamic Simulation

In this Section, simulations in COMSOL of the zinc–nickel RFB were used to visualize the local velocity profiles in the electrolyte flow channel and the electrodes of the battery. The color shades in Figure 6a reflect the magnitude of the velocity vector at a constant inlet flow rate of 0.02 m/s.

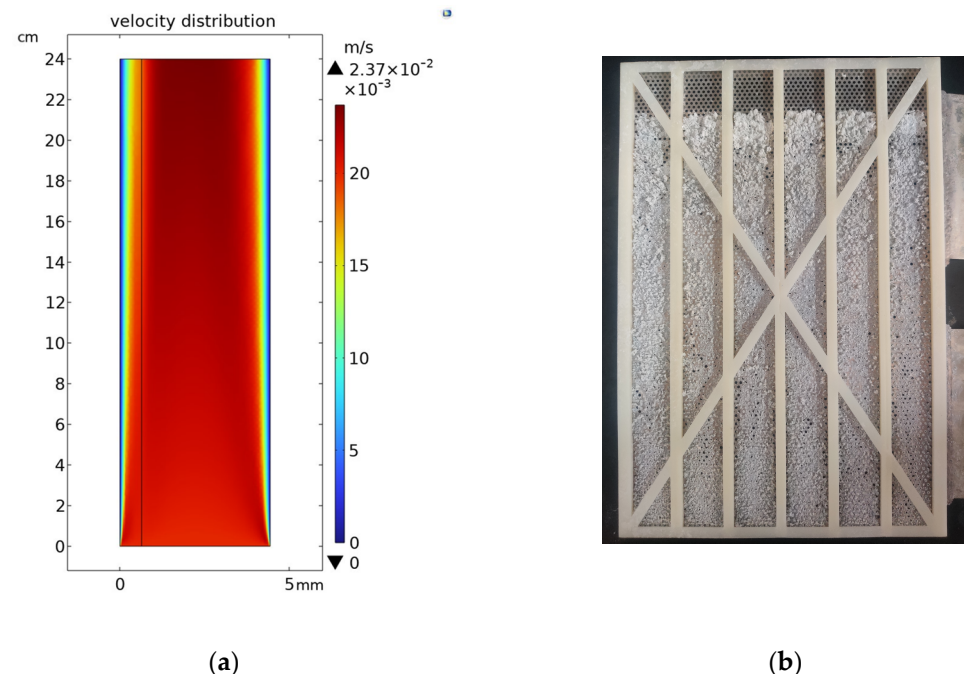


**Figure 6.** (a) Velocity distribution in zinc–nickel RFB operating at 0.02 m/s. (b) Electrode surface after charge/discharge cycle.

It can be clearly observed that with the increase in height, the region where the electrolyte flow velocity is zero, near the negative electrode boundary, gradually widens. This is because at a height of 0, the interface between the negative electrode and the electrolyte undergoes a reaction immediately. As the height increases, the reaction products generated gradually accumulate on the electrode surface, forcing the electrolyte flow to move away from the negative electrode surface. At the same time, due to the constant flow of liquid entering the channel, the thickness of the deposited material on the negative electrode increases, and pressure from the electrode's side grows. Consequently, the velocity at the outlet exceeds that at the inlet, resulting in a deeper color at the outlet compared to the lighter color at the inlet.

For velocity distribution in the porous-positive domain, according to Darcy's law, the flow velocity within a porous medium typically exhibits a decrease as the distance from the flow inlet increases. This phenomenon arises due to the intrinsic resistance encountered by the flow as it traverses through the porous structure. The permeability of the porous medium governs the ease with which the flow can pass through, with higher permeability resulting in lower resistance and vice versa. Consequently, as the flow progresses towards regions distant from the inlet, the cumulative resistance to flow intensifies, leading to a reduction in flow velocity. Thus, it is customary to observe a decline in flow velocity with increasing distance from the flow inlet in scenarios conforming to Darcy's law.

After the experiment, when disassembling the battery prototype, it was observed that the thickness and compactness of the deposited zinc at the outlet were significantly greater than those at the inlet, as Figure 6b shows, evidenced in the simulation results. In Ref. [41], the researchers claimed that in their 3D model, the largest velocity differences occur in the x–y plane, which cannot be observed in a 2D study. However, both studies are identical in that an uneven distribution of electrolyte flow within the channel and porous

domain was observed, which accelerates the degradation of cell components, resulting in a shorter battery lifespan and reduced charge–discharge efficiency. Therefore, designing different morphologies of the negative electrode at different heights to facilitate uniform deposition and stable reaction rates may be a promising direction for the development of a zinc–nickel RFB.

### 3.3. Ion Concentration Distribution

According to the Nernst–Planck equation, mass transfer in electrochemical systems is influenced by three primary mechanisms: diffusion driven by concentration gradients, electromigration driven by electric potential gradients, and convection driven by flow. These factors, along with substance generation and consumption in electrochemical reactions, collectively determine the concentration distribution. Analysis of ion concentration distribution conducted during a constant current charge–discharge ( $20 \text{ mA/cm}^2$ ) at the half height of the model ( $H = 120 \text{ mm}$ ), as Figure 7 depicts, elucidates the dominant factors shaping concentration gradients.

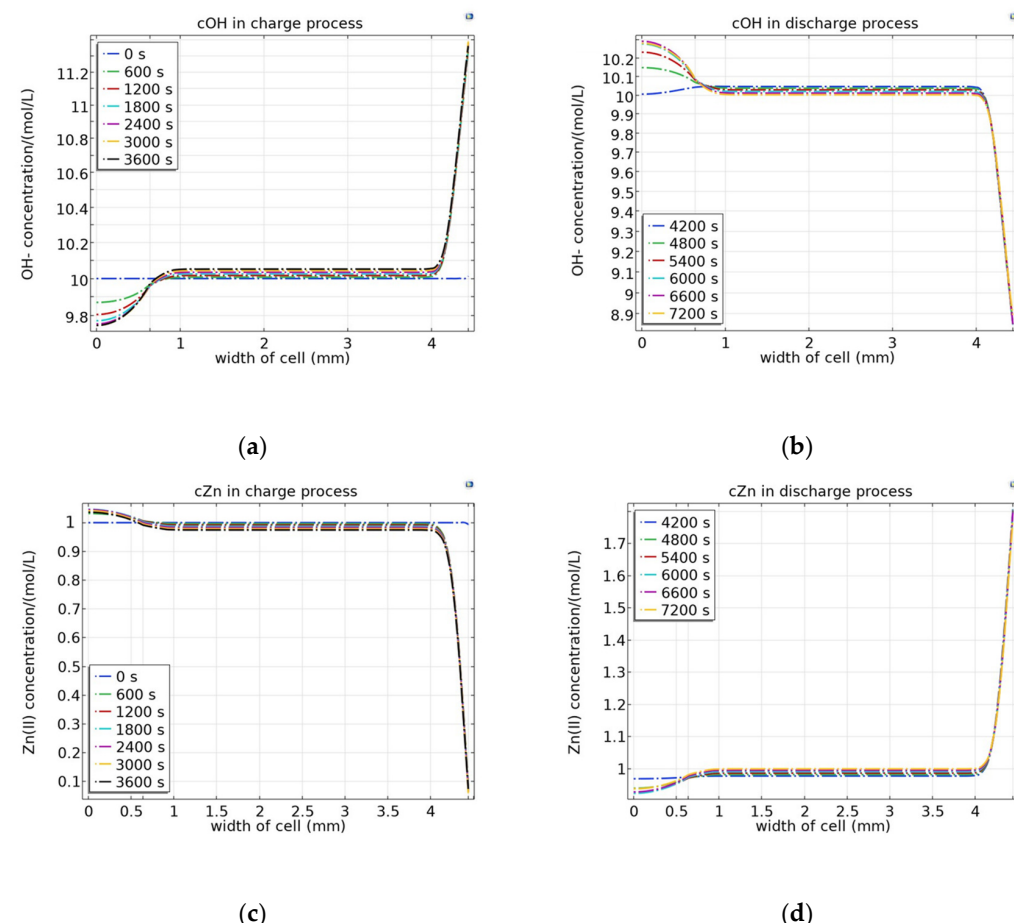


**Figure 7.** Concentration distribution of (a,b)  $\text{OH}^-$  and (c,d)  $\text{Zn}(\text{OH})_4^{2-}$  along the X-axis at half height ( $H = 120 \text{ mm}$ ) during (a,c) charge and (b,d) discharge.

Figure 7 reveals that ion concentration gradients are more pronounced on the surfaces of the porous-positive and -negative electrodes compared to those in the electrolyte channel domain. This disparity arises from higher flow velocities in the electrolyte channel, which primarily drive convective mass transfer, resulting in a more uniform concentration distribution throughout the electrolyte channel domain. Conversely, mass transfer was dominated by diffusion and electromigration in lower flow velocity scenarios, thereby generating larger concentration gradients in the porous domain and on electrode surfaces.

On the negative electrode surface during charging/discharging (Figure 7a,b),  $\text{OH}^-$  generation/consumption induces a concentration gradient, causing ions to diffuse towards lower concentration. Ions migrate towards the electrode surface due to potential gradients in the porous-positive electrode while being consumed by the electrode reaction, leading to a decreasing  $\text{OH}^-$  concentration. Meanwhile, the concentration of  $\text{Zn}(\text{OH})_4^{2-}$  remains stable in the porous-positive domain (Figure 7c,d) since it does not participate in the reactions therein.

Further analysis reveals that the concentration gradient on the negative electrode surface remains relatively constant over time due to the stable electrochemical reactions and minimal potential gradients in the electrolyte flow channel. Conversely, in the porous-positive electrode, increasing potential gradients during charging exacerbates electromigration effects, amplifying ion concentration gradients.

It is clear that the rate of change of concentration at the surface of the negative electrode is much greater than the rate of change in concentration near the positive electrode, which caused by the rapid reaction kinetics of the  $\text{Zn}(\text{OH})_4^{2-}/\text{Zn}$  reaction. The result of such a rapid reaction is that a large number of dendrites will be generated on the electrode surface, as Figure 6b demonstrates. Thus, it may be helpful to make the grown dendrites able to participate in the chemical reaction again by adding additives, or to restrict the reaction rate by alloying with a specific metal.

### 3.4. Current-Potential Behavior in Positive Electrode and Electrolyte

The performance of zinc–nickel RFB batteries relies significantly on the transport processes of active species like ions and electrons to charge transport. These processes dictate the ohmic and concentration losses, which are the primary energy losses during charge–discharge cycles. Figure 8 illustrates the distribution of current density and potential in the porous electrodes and electrolyte. The change in color shades represents the magnitude of the potential gradient, while the density of arrows indicates the distribution of current density. As can be seen, current distribution in the electrolyte channel is more uniform compared to that in the porous medium. This phenomenon is consistent with the mentioned flow velocity distribution pattern. From Figure 8, it is evident that the current density distribution is notably influenced by the flow velocity distribution for the resemblance between the electrolyte flow pattern.

In terms of potential distribution, gradients are primarily observed in the liquid phase potential during the charging phase, where it exhibits a clear proportionality to height, while significant potential gradients are not observed during the discharge process for the liquid phase and the whole process for the solid phase within the porous medium. This implies that, within the porous medium, current density is predominantly influenced by concentration gradients, whereas within the electrolyte flow channel, velocity serves as the primary determinant of current density. Combined with results from Section 3.2, the internal changes in zinc–nickel RFB during the charging and discharging process can be summarized as follows: after activation, zinc deposition occurs on the surface of the negative electrode, and some “dead zinc” grows in the form of dendrites to eventually form a dense layer, which exerts lateral pressure on the flow, resulting in an enlargement of the velocity field near the outlet.

Although the reaction rate of the negative electrode remains relatively constant, the formation of dendritic structures equivalently increases the surface area of the electrode, leading to more sites for zinc deposition and accumulation of inactive materials; the lifespan of battery is shortened, consequently. In addition, the increase in internal resistance reduces the uniformity of current density distribution, with its impact escalating as the height increases. Therefore, height is a crucial factor in battery design, excessive height may even lead to the connection of positive and negative electrodes, causing a short circuit. A V-shaped structure of electrodes pairs may alleviate these issues.

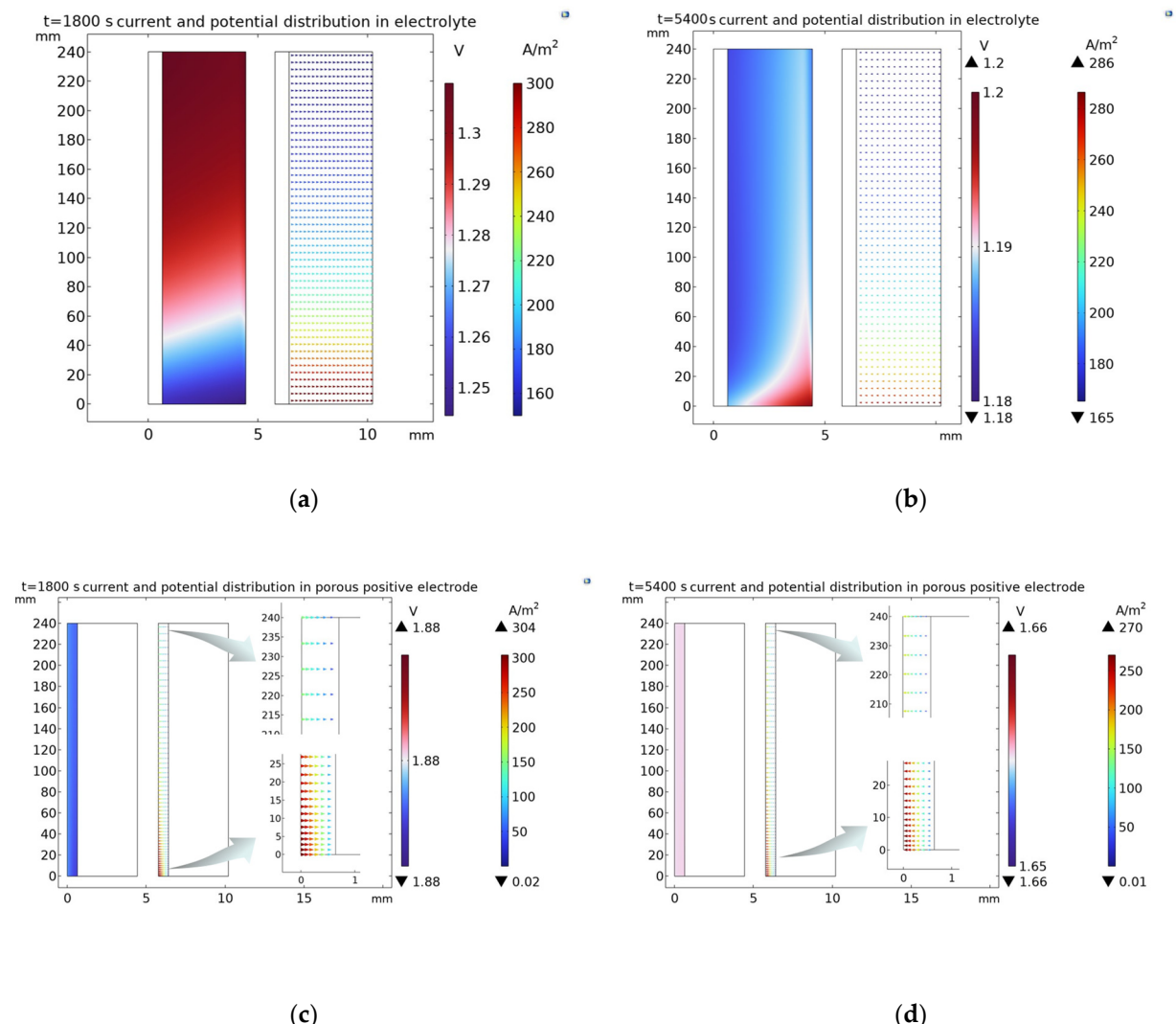


**Figure 8.** Current and potential distribution in the electrolyte: (a) at 1800 s; (b) at 5400 s and porous positive domain: (c) at 1800 s; and (d) at 5400 s operating at  $20 \text{ mA/cm}^2$  with 2 h charge–discharge process.

As was noted at the beginning of this Section, the mass transport losses are closely associated with cell overpotential, which are shown in Figure 9 throughout the circle. Figure 9 illustrates the variation of the overpotentials at the positive electrode boundary, negative electrode boundary, and overpotential difference (the positive electrode boundary to the negative electrode boundary) over time under constant current charge–discharge conditions of  $20 \text{ mA/cm}^2$  in the zinc–nickel RFB battery. From Figure 9, it can be observed that the overpotential at the positive electrode boundary gradually increases during the charging process and sharply decreases during the discharging process, with a more pronounced decrease towards the end of discharge. The overpotential at the negative electrode boundary sharply decreases during the charging process, then decreases slowly, remaining nearly constant during the discharging process. By comparing this with Figure 7, it is evident that the overpotential at the negative electrode boundary correlates strongly with the concentration changes of ions at the negative electrode boundary. The behavior of the zinc–nickel RFB is adequately characterized by both results. A decrease in  $\text{OH}^-$  ion concentration due to reduction correlates with a tendency towards negative overpotential. Conversely, an increase in  $\text{Zn}(\text{OH})_4^{2-}$  ion concentration resulting from Zn oxidation correlates with a tendency towards positive overpotential.

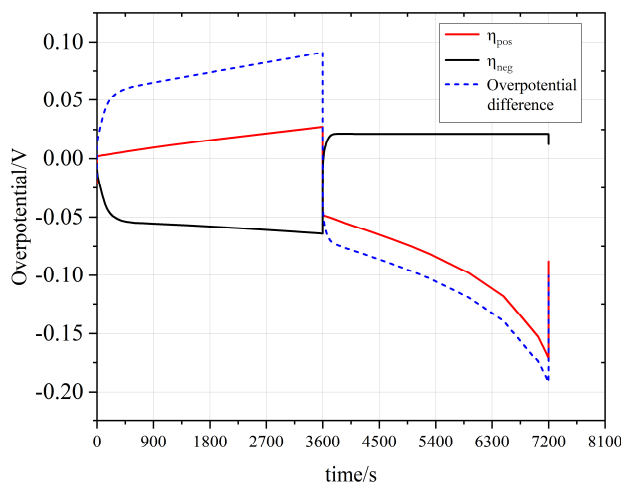


**Figure 9.** Simulated the variation of overpotential over time of zinc–nickel RFB operated at  $20 \text{ mA/cm}^2$  with 2 h charge–discharge process.

These findings support the effectiveness of the proposed model for the zinc–nickel RFB. It demonstrates the capability to accurately describe the current and potential distribution under various operating conditions. Under most battery operating scenarios, the model offers precise predictions of current, negative, and positive electrode potentials, and full output voltages of the battery across single or multiple charge–discharge cycles.

#### 4. Conclusions

In this study, a two-dimensional model was proposed to simulate the zinc–nickel RFB. The model incorporated all three modes of charge transport (migration, diffusion, and convection) coupled with the electrode kinetics of the redox reactions occurring on the electrode surface and within the electrolytes. Charge–discharge curves of the battery were simulated at various current density levels using COMSOL 6.0 and compared with experimental data. As shown by both simulation and experimental data, the internal resistance increased with current density, and the distribution of current and potential was influenced by flow velocity. The concentration gradient on the surface of the negative electrode remained almost unchanged over time, suggesting that the fast kinetics for  $\text{Zn(OH)}_4^{2-}/\text{Zn}$  redox reaction allowed zinc to proceed rapidly all the time at a steady reaction rate, leading to dead zinc deposition, electrode passivation, and reactant inactivation. To limit dendrite growth, the reaction rate must be controlled. However, in porous electrodes, electromigration has a greater impact, resulting in a larger ion concentration gradient. This suggests that the reaction rate of the positive electrode does not match that of the negative electrode, and if we want to build high-capacity batteries with fast charging and discharging characteristics, redesigning the positive electrode may be a better choice.

In summary, this article suggests the following points to improve battery performance:

1. A V-shaped structure and height restriction of electrodes pairs may alleviate the uneven distribution of current density.
2. Limiting the reaction rate of the negative electrode by adding additives or by alloying with specific metals can help to mitigate the growth of dendrites and prolong battery lifespan.
3. Improving the positive electrode to match the reaction rate of the negative electrode may be able to break through the present charging and discharging rate limitations and achieve a faster charge and discharge process.

The proposed model validated with the experimental data mentioned could facilitate the development of high-performance zinc–nickel RFBs and could be extrapolated to optimize the design of other flow batteries.

**Author Contributions:** Conceptualization, C.S.; methodology, K.Z. and N.L.; software, K.Z.; validation, K.Z.; formal analysis, K.Z.; investigation, N.L.; resources, N.L.; data curation, N.L.; writing—original draft preparation, K.Z.; writing—review and editing, K.Z. and C.S.; visualization, K.Z.; supervision, C.S.; project administration, C.S.; funding acquisition, C.S. All authors have read and agreed to the published version of the manuscript.

**Funding:** This research was funded by National Natural Science Foundation of China, grant number 51767005.

**Data Availability Statement:** The original contributions presented in the study are included in the article, further inquiries can be directed to the corresponding author.

**Conflicts of Interest:** The authors declare no conflicts of interest.

## References

1. Dehghani-Sanj, A.R.; Tharumalingam, E.; Dusseault, M.B.; Fraser, R. Study of energy storage systems and environmental challenges of batteries. *Renew. Sustain. Energy Rev.* **2019**, *104*, 192–208. [[CrossRef](#)]
2. Sinsel, S.R.; Riemke, R.L.; Hoffmann, V.H. Challenges and solution technologies for the integration of variable renewable energy sources—A review. *Renew. Energy* **2020**, *145*, 2271–2285. [[CrossRef](#)]
3. Matthew, L.; Tongchao, L.; Xuanxuan, B.; Zhongwei, C.; Khalil, A.; Cheng, Z.; Jun, L. Cationic and anionic redox in lithium-ion based batteries. *Chem. Soc. Rev.* **2020**, *49*, 1688–1705. [[CrossRef](#)] [[PubMed](#)]
4. Ji, X. A paradigm of storage batteries. *Energy Environ. Sci.* **2019**, *12*, 3203–3224. [[CrossRef](#)]
5. Schmidt, O.; Hawkes, A.; Gambhir, A.; Staffell, I. The future cost of electrical energy storage based on experience rates. *Nat. Energy* **2017**, *2*, 17110. [[CrossRef](#)]
6. Yang, S.; Zhang, F.; Ding, H.; He, P.; Zhou, H. Lithium Metal Extraction from Seawater. *Joule* **2018**, *2*, 1648–1651. [[CrossRef](#)]
7. Kostiantyn, T.; Dmitry, B.; Vinod, S.; Gleb, Y. Ten years left to redesign lithium-ion batteries. *Nature* **2018**, *559*, 467–470. [[CrossRef](#)] [[PubMed](#)]
8. Tahil, W. The Trouble with Lithium. Available online: [http://www.meridian-int-res.com/Projects/Lithium\\_Problem\\_2.pdf](http://www.meridian-int-res.com/Projects/Lithium_Problem_2.pdf) (accessed on 3 April 2024).
9. Ahn, H.; Kim, D.; Lee, M.; Nam, K.W. Challenges and possibilities for aqueous battery systems. *Commun. Mater.* **2023**, *4*, 37. [[CrossRef](#)]
10. Fan, X.; Liu, B.; Liu, J.; Ding, J.; Han, X.; Deng, Y.; Lv, X.; Xie, Y.; Chen, B.; Hu, W.; et al. Battery Technologies for Grid-Level Large-Scale Electrical Energy Storage. *Trans. Tianjin Univ.* **2020**, *26*, 92–103. [[CrossRef](#)]
11. Zhao, Z.; Liu, B.; Shen, Y.; Wu, T.; Zang, X.; Zhao, Y.; Zhong, C.; Ma, F.; Hu, W. Comparative study of intrinsically safe zinc-nickel batteries and lead-acid batteries for energy storage. *J. Power Sources* **2021**, *510*, 230393. [[CrossRef](#)]
12. Zhang, X.; Lv, R.; Tang, W.; Li, G.; Wang, A.; Dong, A.; Liu, X.; Luo, J. Challenges and Opportunities for Multivalent Metal Anodes in Rechargeable Batteries. *Adv. Funct. Mater.* **2020**, *30*, 2004187. [[CrossRef](#)]
13. Liang, Y.; Yao, Y. Designing modern aqueous batteries. *Nat. Rev. Mater.* **2022**, *8*, 109–122. [[CrossRef](#)]
14. Wang, T.; Li, C.; Xie, X.; Lu, B.; He, Z.; Liang, S.; Zhou, J. Anode Materials for Aqueous Zinc Ion Batteries: Mechanisms, Properties, and Perspectives. *ACS Nano* **2020**, *14*, 16321–16347. [[CrossRef](#)] [[PubMed](#)]
15. Martin, W.; Brian, B.; Kang, X. Before Li Ion Batteries. *Chem. Rev.* **2018**, *118*, 11433–11456. [[CrossRef](#)] [[PubMed](#)]
16. Li, Z.; Lu, Y. Material Design of Aqueous Redox Flow Batteries: Fundamental Challenges and Mitigation Strategies. *Adv. Mater.* **2020**, *32*, e2002132. [[CrossRef](#)] [[PubMed](#)]
17. Yaroshevsky, A.A. Abundances of Chemical Elements in the Earth’s Crust. *Geochem. Int.* **2006**, *44*, 48–55. [[CrossRef](#)]
18. Li, C.; Xie, X.; Liang, S.; Zhou, J. Issues and Future Perspective on Zinc Metal Anode for Rechargeable Aqueous Zinc-ion Batteries. *Energy Environ. Mater.* **2020**, *3*, 146–159. [[CrossRef](#)]
19. Cheng, J.; Zhang, L.; Yang, Y.-S.; Wen, Y.-H.; Cao, G.-P.; Wang, X.-D. Preliminary study of single flow zinc–nickel battery. *Electrochem. Commun.* **2007**, *9*, 2639–2642. [[CrossRef](#)]
20. Cheng, Y.; Zhang, H.; Lai, Q. High Power Density Zinc-nickel Single Flow Batteries with Excellent Performance. *ECS Trans.* **2014**, *59*, 3–7. [[CrossRef](#)]
21. Chen, T.; Wang, F.; Cao, S.; Bai, Y.; Zheng, S.; Li, W.; Zhang, S.; Hu, S.X.; Pang, H. In situ synthesis of MOF-74 family for high areal energy density of aqueous nickel–zinc batteries. *Adv. Mater.* **2022**, *34*, 2201779. [[CrossRef](#)]
22. Wang, Q.; Liu, X.; Wang, H.; Shen, Y.; Zhao, Z.; Zhong, C.; Hu, W. Ti4O7 regulating both  $Zn(OH)_4^{2-}$  and electrons for improving Zn-Ni batteries. *Chem. Eng. J.* **2022**, *443*, 136342. [[CrossRef](#)]
23. Wang, S.; Yuan, C.; Chang, N.; Song, Y.; Zhang, H.; Yin, Y.; Li, X. Act in contravention: A non-planar coupled electrode design utilizing “tip effect” for ultra-high areal capacity, long cycle life zinc-based batteries. *Sci. Bull.* **2021**, *66*, 889–896. [[CrossRef](#)]
24. Tang, L.; Dai, S.; Leung, P.; Mohamed, M.R.; Zeng, Y.; Zhu, X.; Flox, C.; Shah, A.A.; Liao, Q. Exploring the Performance and Mass-Transfer Characteristics of Porous Zinc Anodes for Membraneless Hybrid-Flow Batteries. *Batteries* **2023**, *9*, 340. [[CrossRef](#)]
25. Huang, X.; Yao, S.; Yang, X.; Sun, X.; Zhou, R.; Liu, X.; Cheng, J. Polarization analysis and optimization of negative electrode nickel foam structure of zinc-nickel single-flow battery. *J. Energy Storage* **2022**, *55*, 105624. [[CrossRef](#)]

26. Lei, X.; Ma, Z.; Bai, L.; Wang, L.; Ding, Y.; Song, S.; Song, A.; Dong, H.; Tian, H.; Tian, H. Porous ZnP matrix for long-lifespan and dendrite-free Zn metal anodes. *Battery Energy* **2023**, *2*, 20230024. [[CrossRef](#)]
27. Wang, S.; Li, T.; Yin, Y.; Chang, N.; Zhang, H.; Li, X. High-energy-density aqueous zinc-based hybrid supercapacitor-battery with uniform zinc deposition achieved by multifunctional decoupled additive. *Nano Energy* **2022**, *96*, 107120. [[CrossRef](#)]
28. Zhang, Z.; Shen, Y.; Zhao, Z.; Li, S.; Wang, Q.; Zhong, C.; Hu, W. Organic additives in alkaline electrolyte to improve cycling life of aqueous Zn–Ni batteries. *J. Power Sources* **2022**, *542*, 231815. [[CrossRef](#)]
29. Shen, Y.; Wang, Q.; Liu, J.; Zhong, C.; Hu, W. Spontaneous reduction and adsorption of K<sub>3</sub>[Fe(CN)<sub>6</sub>] on Zn anodes in alkaline electrolytes: Enabling a long-life Zn–Ni battery. *Acta Phys.-Chim. Sin.* **2022**, *38*, 2204048. [[CrossRef](#)]
30. Yao, S.; Kan, X.; Zhou, R.; Ding, X.; Xiao, M.; Cheng, J. Simulation of dendritic growth of a zinc anode in a zinc–nickel single flow battery using the phase field-lattice Boltzmann method. *New J. Chem.* **2021**, *45*, 1838–1852. [[CrossRef](#)]
31. Huang, X.; Yao, S.; Zhou, R.; Yang, X.; Kan, X.; Cheng, J. Study on the effect of hydrogen evolution reaction in the zinc–nickel single flow battery. *J. Energy Storage* **2022**, *50*, 104246. [[CrossRef](#)]
32. Yao, S.; Liao, P.; Xiao, M.; Cheng, J.; He, K. Modeling and simulation of the zinc–nickel single flow batteries based on MATLAB/Simulink. *AIP Adv.* **2016**, *6*, 125302. [[CrossRef](#)]
33. Yao, S.; Liao, P.; Xiao, M.; Cheng, J.; He, K. Equivalent circuit modeling and simulation of the zinc nickel single flow battery. *AIP Adv.* **2017**, *7*, 055112. [[CrossRef](#)]
34. Rong, S.; Ma, J.; Zhang, H.; Yu, J.; Wang, T.; Cai, Y.; Han, Z.; Ji, Y. Potential prediction in aqueous organic redox-targeting flow batteries: DFT calculation and experimental validation. *Energy Storage Mater.* **2024**, *69*, 103389. [[CrossRef](#)]
35. Huang, X.; Zhou, R.; Luo, X.; Yang, X.; Cheng, J.; Yan, J. Experimental research and multi-physical modeling progress of Zinc-Nickel single flow battery: A critical review. *Adv. Appl. Energy* **2023**, *12*, 100154. [[CrossRef](#)]
36. Guo, X.; He, G. Opportunities and challenges of zinc anodes in rechargeable aqueous batteries. *J. Mater. Chem. A* **2023**, *11*, 11987–12001. [[CrossRef](#)]
37. Lide, D.R. *CRC Handbook of Chemistry and Physics*; CRC Press: Boca Raton, FL, USA, 2004; Volume 85.
38. Amini, K.; Pritzker, M.D. A two-dimensional transient model for a zinc-cerium redox flow battery validated by extensive experimental data. *J. Power Sources* **2021**, *506*, 230237. [[CrossRef](#)]
39. Song, C.; Zhang, Y.; Ling, Q.; Zheng, S. Joint estimation of soc and soh for single-flow zinc–nickel batteries. *Energies* **2022**, *15*, 4781. [[CrossRef](#)]
40. Xu, S.; Huang, J.; Wang, G.; Dou, Y.; Yuan, D.; Lin, L.; Qin, K.; Wu, K.; Liu, H.K.; Dou, S.X.; et al. Electrolyte and Additive Engineering for Zn Anode Interfacial Regulation in Aqueous Zinc Batteries. *J. Small Methods* **2023**. [[CrossRef](#)]
41. Aparicio-Mauricio, G.; Jiménez-Lima, L.; Rivero, E.P.; Cruz-Díaz, M.R. 3D modeling and simulation of an alkaline flow battery considering the tertiary current distribution on the electrodes: Anthraquinone-ferro/ferricyanide as organic electroactive species. *J. Power Sources* **2023**, *582*, 233533. [[CrossRef](#)]

**Disclaimer/Publisher’s Note:** The statements, opinions and data contained in all publications are solely those of the individual author(s) and contributor(s) and not of MDPI and/or the editor(s). MDPI and/or the editor(s) disclaim responsibility for any injury to people or property resulting from any ideas, methods, instructions or products referred to in the content.